IOP Publishing Phys. Med. Biol. 65 (2020) 195002 https://doi.org/10.1088/1361-6560/abb02c

Physics in Medicine & Biology

IPEM Institute of Physics and Engineering in Medicine

PAPER

Truncation compensation and metallic dental implant artefact reduction in PET/MRI attenuation correction using deep learning-based object completion

RECEIVED
14 May 2020

REVISED
11 August 2020

ACCEPTED FOR PUBLICATION
18 August 2020

PUBLISHED
22 September 2020

Hossein Arabi[1] **and Habib Zaidi**[1,2,3,4]

[1] Division of Nuclear Medicine and Molecular Imaging, Department of Medical Imaging, Geneva University Hospital, Geneva 4, CH-1211, Switzerland
[2] Geneva University Neurocenter, Geneva University, Geneva, CH-1205, Switzerland
[3] Department of Nuclear Medicine and Molecular Imaging, University of Groningen, University Medical Center Groningen, RB Groningen, 9700, The Netherlands
[4] Department of Nuclear Medicine, University of Southern Denmark, Odense, DK-500, Denmark

E-mail: habib.zaidi@hcuge.ch

Keywords: PET/MRI, metal artefact reduction, body truncation, deep learning, quantitative PET

Abstract

The susceptibility of MRI to metallic objects leads to void MR signal and missing information around metallic implants. In addition, body truncation occurs in MR imaging for large patients who exceed the transaxial field-of-view of the scanner. Body truncation and metal artefacts translate to incomplete MRI-derived attenuation correction (AC) maps, consequently resulting in large quantification errors in PET imaging. In this work, we propose a deep learning-based approach to predict the missing information/regions in MR images affected by metallic artefacts and/or body truncation aiming at reducing quantification errors in PET/MRI. Twenty-five whole-body (WB) co-registered PET, CT, and MR images were used for training and evaluation of the object completion approach. CT-based attenuation corrected PET images were considered as reference for the quantitative evaluation of the proposed approach. Its performance was compared to the 3-class segmentation-based AC approach (containing background air, soft-tissue and lung) obtained from MR images. The metal-induced artefacts affected $8.1 \pm 1.8\%$ of the volume of the head region when using the 3-class AC maps. This error reduced to $0.9 \pm 0.5\%$ after application of object completion on MR images. Consequently, quantification errors in PET images reduced from $-57.5 \pm 11\%$ to $-18.5 \pm 5\%$ in the head region after metal artefact correction. The percentage of the torso volume affected by body truncation in the 3-class AC maps reduced from $9.8 \pm 1.9\%$ to $0.6 \pm 0.3\%$ after truncation compensation. PET quantification errors in the affected regions were also reduced from $-45.5 \pm 10\%$ to $-9.5 \pm 3\%$ after truncation compensation. The quantitative results demonstrated promising performance of the proposed approach towards the completion of MR images corrupted by metal artefacts and/or body truncation in the context of WB PET/MR imaging.

1. Introduction

Hybrid PET/MRI emerged as a promising imaging technology for basic and clinical research applications (Zaidi and Becker 2016). However, although a countless number of works have been reported in the literature, attenuation correction (AC) is still considered one of the major challenges facing quantitative whole-body (WB) PET/MR imaging (Mehranian *et al* 2016b). A common practice to create AC maps for AC in PET/MRI is bulk classification/segmentation of MR images into a number of predefined tissue classes followed by assignment of corresponding linear attenuation coefficients (Martinez-Moller *et al* 2009, Schulz *et al* 2011, Ouyang *et al* 2013, Arabi *et al* 2015). Delineation of the body contour and correct identification of the different organs and/or tissues play a key role in the accuracy of MRI segmentation-based AC map

generation. In this regard, MR images affected by noticeable image artefacts can potentially impair the accuracy of segmentation-based AC map generation. Such artefacts are commonly observed in patients bearing dental and/or metal implants, wherein the MR magnetic field susceptibility to the presence of metallic objects gives rise to faded signals or void areas in the corresponding MR images (Schramm and Ladefoged 2019).

In hybrid PET/MRI scanners, the MR imaging transaxial field-of-view (FOV) is smaller than that of PET imaging (Schramm *et al* 2013). Hence, the incomplete MR image of the body, particularly the truncated arms of large patients, would result in incomplete MRI-derived AC maps wherein parts of the arms/body are missing. In this regard, various MR sequences, such as multi-acquisition variable resonance image combination (MAVRIC) (Burger *et al* 2015) and B_0 homogenization using the gradient enhancement (HUGE) sequences have been proposed to extend the FOV of MR images for full body coverage or at least reduce the adverse impact of truncation errors (Lindemann *et al* 2017).

To address body truncation and complete the missing parts in MRI-derived AC maps, delineation of the body contour on uncorrected time-of-flight (TOF) PET (PET-nonAC) images has also been proposed (Qian *et al* 2012). This approach relies on the strong signals at the boundary of the body provided by TOF PET reconstruction. However, this method is applicable mainly to radiotracers with sufficient uptake on the boundary of the body. Alternatively, the missing part of the MR-derived attenuation map can be compensated via joint reconstruction of the attenuation and activity maps, wherein the PET emission data (preferably with TOF information) is used to estimate the most likely attenuation map corresponding to the emission data (Nuyts *et al* 2013).

The void signal in MR images owing to the presence of metal implants or body truncation may notably impair tissue classification and/or delineation of the body contour for AC map generation (Blumhagen *et al* 2014). This commonly translates in incomplete AC maps up to 5 l in volume, consequently leading to more than 50% underestimation of the tracer uptake within the affected areas (Qian *et al* 2012, Arabi and Zaidi 2016a). A number of strategies were devised to address this issue, including region-specific optimization of continuous linear attenuation coefficients based on ultrashort echo sequence (RESOLUTE) (Ladefoged *et al* 2017). The same joint reconstruction of attenuation and activity mentioned above was also used to resolve the position, shape, and attenuation coefficients of metallic implants (Fuin *et al* 2017).

In this work, a deep learning-based approach is proposed to simultaneously tackle body truncation and metal artefacts in WB PET/MRI. The deep learning network is trained using complete non-affected MR images (without truncation or metal artefacts) to learn the filling/completion of the missing parts (patches of voxels). Subsequently, this model is employed to accomplish shape completion on metal artefact affected or truncated MR images. The quantitative performance of the proposed approach is evaluated using clinical WB PET/CT/MR studies.

2. Materials and methods

2.1. Data acquisition

The cohort used in this study consisted of 25 WB clinical ^{18}F-FDG PET/MRI scans followed by ^{18}F-FDG PET/CT examinations for staging and follow-up assessment of head and neck malignancies using a single radiotracer injection. The cohort consisted of 18 men and 7 women with a mean age of 65 (50–77) yr and mean weight of 79 (59–104) kg. The study protocol was approved by Geneva Cantonal Research ethics committee. WB MRI examinations (Dixon 3D volumetric interpolated T1-weighted sequence) were carried out as part of the PET/MRI protocol on the Ingenuity TF PET/MRI system (Philips Healthcare, Cleveland, OH) using TE 11.1 ms, flip angle 10°, transverse FOV of 450 × 354 mm^2, and voxel size 0.85 × 0.85 × 3 mm^3. Shortly afterward, the patients underwent ^{18}F-FDG PET/CT scans on a Biograph 64 True Point scanner (Siemens Healthcare, Erlangen, Germany) 126 ± 10 min post-injection of 369 ± 22 MBq^{18}F-FDG. The PET acquisitions were performed in 5–6 bed positions lasting 3 min per bed position. Unenhanced CT scans performed with 180 mAs, 120 kVp, and a pitch of 1.2 were used for PET AC. The Ingenuity TF PET/MRI scanner relies on the segmentation-based approach to generate a 3-class AC map (consisting of background air, lung, and soft-tissue) for PET AC (Schulz *et al* 2011, Zaidi *et al* 2011). The 3-class AC map is also evaluated in this study as a common AC approach used in clinical practice.

MR Dixon images acquired on the Ingenuity TF PET/MR scanner were co-registered to CT images. Image registration was carried out via a combination of rigid and non-rigid alignment using normalized mutual information as loss function, B-spline interpolator, and adaptive stochastic gradient descent optimizer. Prior to image co-registration, all MR images underwent N4 bias correction (to reduce the low-frequency intensity non-uniformity within each image) and inter-subject histogram matching to reduce the intensity variation across different subjects. All MR images were normalized by their own maximum voxel value to render a voxel intensity ranging from 0 to 1. As a result of image registration, the MR images

Table 1. Shape, size and location of the void areas created in the MR images to simulate metallic-artefacts and body truncation.

	Location	Shape	Size
Body truncation	Arms Left side only Right side only Both sides with symmetry Both sides without symmetry	Rectangular cuboid	Length: covering the entire length of the patient arms Width: 3–15 cm
Metal-artefacts	Mandible & Upper jaw (single void area per patient)	Cube Sphere Cylinder Rectangular cuboid	Volume: 8–128 cm^3

were mapped to a matrix size of 512 × 512 × 205–207 voxels at a resolution of 1.36 × 1.36 × 2.5 mm of CT images prior to training of the model.

Fifteen out of the 25 MR images of the patients did not bear any noticeable body truncation or metal-induced artefacts. These were employed for the training of the deep learning approach. Ten patients with MR images affected by body truncation and/or metal-induced artefacts were used for evaluation of the proposed algorithm. The reference (ground-truth) body contours and/or AC maps were generated from the co-registered CT images.

2.2. Deep learning-based approach

To tackle body truncation and metal-induced artefacts (translated to a void region) in MR images, a deep learning-based object completion approach is proposed to learn filling/completing the missing regions. To this end, the deep convolutional neural network was trained considering the unaffected MR images, wherein a variety of artificial body truncations and void areas (mimicking metal-artefacts) were created to train the object completion model. To this end, a high-resolution dilated convolutional neural network with residual connections (Li *et al* 2017) implemented in the open-source NiftyNet platform (Gibson *et al* 2018) was employed. This network consists of 20 residual convolutional layers where 3 × 3 × 3 kernels dilated by factors of 1, 2 and 4 were exploited to capture low-, mid-, and high-level features of the input images, respectively.

The training of the object completion model was carried out using a three-dimensional scheme, wherein at each iteration, a stack of 40 slices of MR images (covering 10 cm of the axial FOV) was considered as a training sample. An axial coverage of 10 cm was selected to take the samples from the input MR images to provide the deep learning algorithm with adequate anatomical information around the affected areas for accurate prediction of the missing parts. Moreover, this axial coverage was large enough to encompass the complete void area induced by metal artefacts and larger axial coverage (more than 10 cm) did not lead to improvement in outcome. Though this axial coverage is not large enough to encompass the whole truncated area, the overlap of 50% used between sample volumes enables to avoid discontinuity in the resulting MR images. Random body truncation and creation of void areas (mimicking the impact of metal-induced artefacts) were performed on the 15 unaffected subjects to build the training dataset. Different masks, in terms of size and shape, were placed on MR images over areas where metal-artefacts and body truncation are more likely to occur. The simulation of body truncation is straightforward as this artefact usually occurs in the arms. Hence, the simulation of truncation artefact was carried by eroding/cutting the patient's arms using different sizes varying from 3 cm to 15 cm from only the left or right side or both sides. The simulation of metallic-artefacts could be much more variable in size and shape as well as anatomical location. In this work, metal-artefact simulation/correction was only performed for dental implants using different shapes and sizes as summarized in table 1. In total 6000 three-dimensional training samples were created from the 15 unaffected subjects. The NiftyNet pipeline version 6.0 built upon TensorTlow platform version 1.12 was employed to build the object completion model, wherein a root-mean-square error (RMSE) loss function (equation (1)) was exploited along with Adam optimization and a learning rate ranging from 0.05 to 0.01 following the optimization procedure described in (Smith 2018). For early iterations, larger learning rates (0.05 and 0.04) were set to facilitate coarse training of the network. For the last epoch, the learning rate decreased to 0.01 to achieve fine training of the model.

$$\mathrm{RMSE} = \sqrt{\sum_{t=1}^{T} \frac{(P_t - R_t)^2}{T}}, \tag{1}$$

where P_t and R_t denote the predicted and reference patches of images at voxel t and T is the total number of voxels in a training sample (stack of 40 slices). A batch size = 6, sample per volume = 1, and decay factor = 0.0001 were selected for the training. The decay factor (λ) determines the regularization of the trainable parameters (w), wherein a ridge regression function (equation (2)) was used to avoid overfitting.

$$\text{Loss\_value}_{\text{regularized}} = \text{Loss\_value}_{\text{initial}} + \lambda \times \text{sum}(w)^2. \quad (2)$$

For the last epoch, the decay factor was set to zero to facilitate the fine training of the model. Regarding the batch size of 6, the training of the model was performed on Intel(R) Xeon 2.30 GHz 7i CPU and 64 GB RAM. Owing to the limited memory of graphic cards, the training and inference of the mode were performed on a single CPU. The training of the model took about 65 h and the loss function reached its plateau after 12 epochs. For the test images, the prediction of the missing parts took about 20 s for each patient.

The validation of the model was carried out on 10 MR images bearing body truncation and/or metal-induced artefacts. Body truncation artefacts in the validation dataset (real patients) occurred slightly asymmetrically in both arms. The volumes of body truncation varied from 360 to 2000 cm^3. Metallic artefacts were induced by dental implants creating void volumes varying between 10 and 110 cm^3. The ground-truth body contours for these 10 MR images were generated from the co-registered CT images.

2.3. Evaluation strategy

To quantify the impact of body truncation and metal-induced artefacts in WB PET/MR imaging, a 3-class AC map was generated from MR images before and after application of the object completion approach. The 3-class AC map consists of background-air, lung, and soft-tissue to which the following attenuation coefficients were assigned: 0 cm^{-1}, 0.022 cm^{-1}, and 0.098 cm^{-1}, respectively. Body truncation and metal-artefacts cause incomplete volume of the body in the AC map. Hence, the percentage of the recovered volume in the MRI-derived AC maps were calculated separately for metal-artefacts (single bed position in the head region) and body truncation (upper- and mid-trunk of body).

For quantitative assessment of PET images, PET data were reconstructed three times, namely using CT AC map to generate reference PET/CT images, the 3-class AC map before correction (PET/MR AC), and 3-class AC map after correction (PET/MRCr AC). Considering PET/CT images as reference, the quantification bias of the standard uptake value (SUV) (%) was calculated for the affected regions in the PET/MRI and PET/MRCr AC images using equation (3). The mean SUV in the area affected by either metal or body truncation artefacts (void areas in the AC map) was used to calculate the SUV bias. To generate reference PET AC maps and calculate the ground truth body volumes, metal artefact reduction (MAR) using the normalized MAR (NMAR) algorithm (Meyer *et al* 2010) was applied to CT images considered as reference for evaluation.

$$\text{SUV Bias } (\%) = \frac{\text{PET/MR (SUV)} - \text{PET/CT (SUV)}}{\text{PET/CT (SUV)}} \times 100\%. \quad (3)$$

3. Results

For qualitative assessment, MR images without body truncation underwent artificial truncation through masking parts of the arms. Subsequently, the object completion approach was used to recover the missing parts of the body. Figure 1 illustrates an example, wherein the MR images before and after compensation of body truncation are presented. The original MR (before artificial body truncation) and the corresponding CT images are also provided for visual inspection of quality/accuracy of the truncation compensation.

Figure 2 shows a representative clinical study showing body truncation error occurring on PET/MR images, wherein the incomplete/truncated arms in the MR image are reflected in the corresponding 3-class AC. The MR image after compensation of body truncation and its corresponding 3-class AC map along with the reference CT image without truncation error are also displayed. The impact of body truncation is visible on PET/MR AC (PET corrected for attenuation using the 3-class technique before truncation compensation) compared to PET/CT AC and PET/MRCr AC (PET corrected for attenuation using the 3-class technique after truncation compensation). The affected regions were determined through the comparison of body contours obtained from the reference CT images and the corresponding 3-class AC maps generated from MR images before correction. The results were then verified visually. The horizontal profiles plotted over PET images portray clearly the underestimation of the activity concentration within the arms region in the PET/MR AC image.

Table 2 summarizes the results for 10 patients presenting with body truncation errors, reporting the percentage of the truncated volume from MR images in the 3-class AC maps for the torso (upper- and mid-trunk of body without head), considering the body volume obtained from CT images as reference.

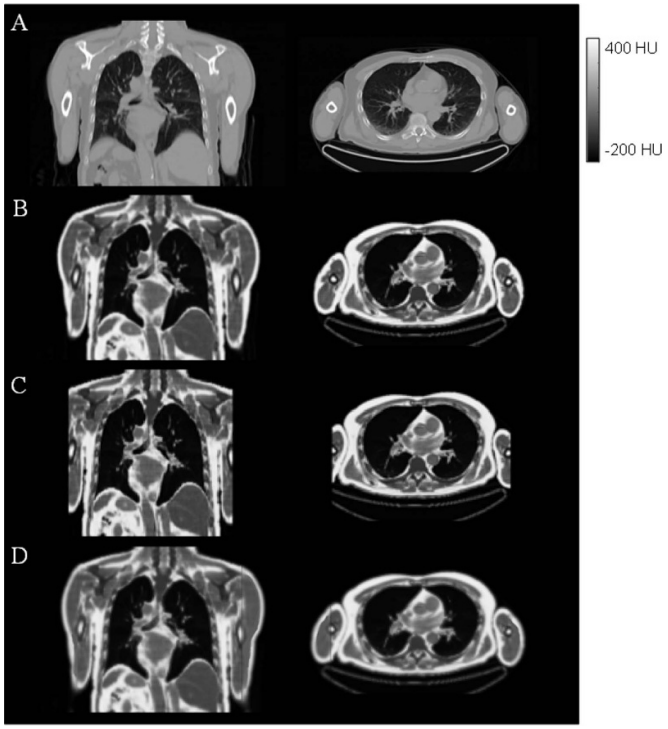

Figure 1. Representative example of a clinical study showing the principle of body truncation compensation. (A) CT image. MR images (B) before artificial body truncation (used as reference), (C) after artificial body truncation, and (D) after truncation compensation.

Table 2. Percentage of the truncated volume in MRI-derived 3-class AC map before and after compensation of body truncation. SUV_{mean} and SUV bias (%) measured in the affected regions are also reported. *p*-Values are calculated between the results of MR AC and MRCr AC approaches.

Body trunk	Truncated volume	SUV_{mean}	SUV bias
CT AC	–	0.75 ± 0.2	–
MR AC	$9.8 \pm 1.9\%$	0.32 ± 0.1	$-45.5 \pm 10\%$
MRCr AC	$0.6 \pm 0.3\%$	0.69 ± 0.2	$-9.5 \pm 3\%$
p-Value	<0.01	<0.02	<0.01

Table 3. Percentage of the truncated volume in MRI-derived 3-class AC map before and after compensation of body truncation. SUV_{mean} and SUV bias (%) calculated in the affected regions are also reported. *p*-Values are calculated between the results of MR AC and MRCr AC approaches.

Head	Affected volume	SUV_{mean}	SUV bias
CT AC	–	1.7 ± 0.4	–
MR AC	$8.1 \pm 1.8\%$	0.5 ± 0.2	$-57.5 \pm 11\%$
MRCr AC	$0.9 \pm 0.5\%$	1.2 ± 0.3	$-18.5 \pm 5\%$
p-Value	<0.01	0.01	<0.01

Significant underestimation of SUV (−45.5%) was observed within the affected regions in PET/MR images, which decreased to −9.5% after applying the object completion method (in PET/MRCr images).

Figure 3 depicts an object completion example of an MR image masked in the jaw area mimicking metal artefact void. The head contour as well as some anatomical details have been well recovered after correction. Figure 4 illustrates a representative metal artefact error occurring in PET/MRI, wherein the incomplete/void area in the MR image is reflected in the corresponding 3-class AC. The head contour was properly recovered in the 3-class AC map after compensation. The horizontal profiles plotted on PET images over the affected area show substantial underestimation and recovery of the activity concentration before and after object completion.

Table 3 summarizes the percentage of the affected (void) volume from MR images in the 3-class AC maps for the head region across 10 patients. SUV underestimation of −57.5% was observed within the void regions in PET/MR images, reducing to −18.5% after object completion in PET/MRCr images.

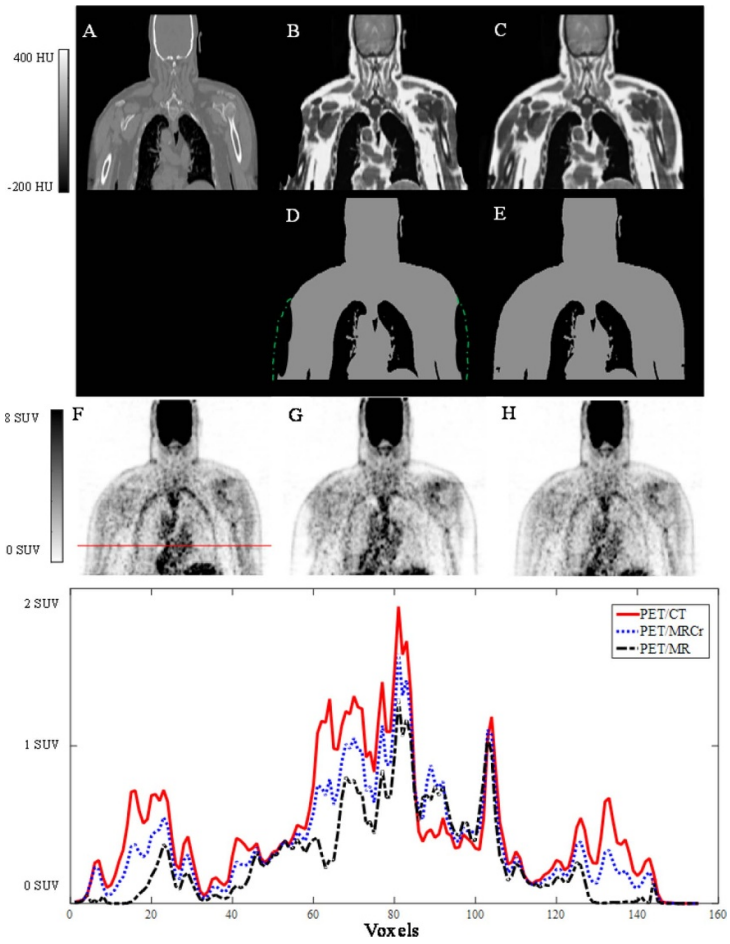

Figure 2. Representative clinical case of body truncation in PET/MRI. (A) CT image, MR images (B) before and (C) after truncation compensation, 3-class AC maps obtained from (D) truncated MR image (B) and (E) MR image after correction (C). The green dashed line indicates the affected/missing regions. PET images corrected for attenuation using (F) CT AC map, (G) 3-class MR AC (PET/MR), and (H) 3-class AC map after truncation compensation (PET/MRCr). The horizontal profiles over the PET images are also displayed.

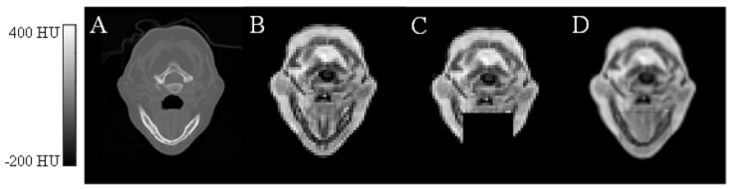

Figure 3. Example of metal artefact compensation. (A) CT image, MR images (B) before inserting the artificial metal artefact (reference), (C) after inserting the artificial metal artefact, and (D) after metal artefact correction.

4. Discussion

Object completion algorithms are widely used in natural image processing to recover semantic structures in the missing/corrupted regions. Similar concepts could be exploited in medical imaging, particularly for cases where seminal structures in the missing regions belong to a specific type of anatomy/morphology, such as the arms in body truncation, which makes it easier to predict. This work attempted to emphasize for the first time the applicability of deep learning-based object completion in medical imaging, however similar ideas have been applied to predict three-dimensional synthetic CT images from a single two-dimensional projection (Shen *et al* 2019). The focus of this study was on MR images in the context of MRI-guided PET attenuation map generation since this type of information loss (truncation and metal artefact) are commonly observed in PET/MRI, thus impacting the quantitative accuracy of PET imaging. In this regard, a

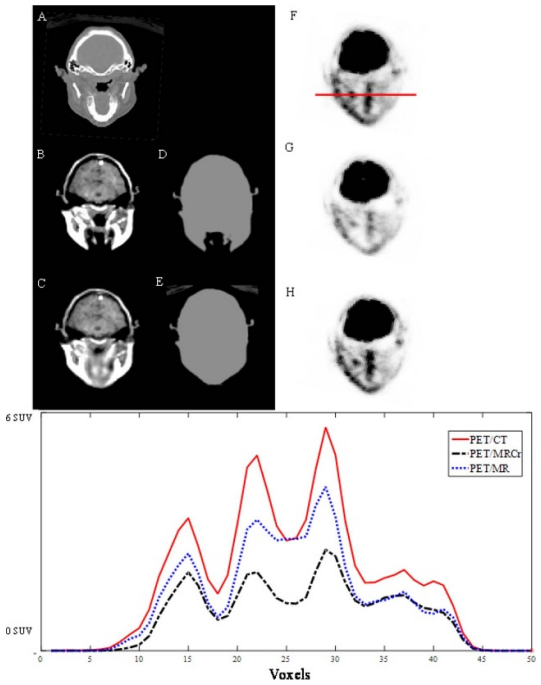

Figure 4. Example of a clinical study showing a case with metal-induced artefacts in PET/MRI. (A) CT image, MR images (B) before and (C) after metal artefact correction, 3-class AC maps obtained from (D) affected MRI shown in (B) and (E) MR image after artefact correction of MRI shown in (C). PET images corrected for attenuation using (F) CT AC map, (G) 3-class MR AC (PET/MR), and (H) 3-class AC map after artefact correction (PET/MRCr). The horizontal profiles over PET images are also displayed.

similar idea can be applied to address metal-induced artefacts in CT imaging (Abdoli *et al* 2016) or halo-artefacts in ^{68}Ga-labelled PSMA-PET imaging (Heußer *et al* 2017).

The head and body contours in 3-class AC maps after applying object completion (MRCr) bear only slight errors in terms of affected volume, yet, quantitative PET analysis showed significant difference between PET-CT AC and PET-MRCr AC images. It should be noted that a large part of this difference is attributed to the lack of bony structures in the 3-class AC maps, which resulted in noticeable underestimation of SUV in PET-MRCr images.

Body truncation and metal artefacts in MR images commonly translate into incomplete MRI-derived PET attenuation maps, particularly when segmentation-based methods are employed. The body contour completion algorithm could also be applied directly on the resulting attenuation maps instead of the original MR images. However, since the original MR images contain plenty of anatomical details and information associated with seminal structures in the missing regions, it is expected that the object completion method performs better when applied on the original MR images, though this claim should be verified. Moreover, MR images, in the context of PET/MR imaging and MRI-only radiation therapy, are also utilized by atlas-based methods (Arabi and Zaidi 2016a), MRI-guided joint activity and attenuation reconstruction algorithms (Mehranian *et al* 2016a, Fuin *et al* 2017, Hwang *et al* 2019), dose estimation in MRI-only radiation planning (Arabi *et al* 2018), low-dose PET imaging (Chen *et al* 2019), deep learning-based synthetic CT generation (Arabi *et al* 2019), synergistic PET and MR image reconstruction (Mehranian *et al* 2019), and segmentation of anatomical structures (Arabi and Zaidi 2016b). The proposed method would also be applicable to continuous-valued AC maps generation from Dixon fat/water sequences (Wollenweber *et al* 2013) to accurately estimate the ratio/fraction of fat and water tissues in the missing regions. However, the training of the proposed method should be repeated on both fat-only and water-only images (rather than IP images) to reach the peak performance for this specific application. Body truncation and metal artefact correction through an object completion framework on MR images could possibly improve the performance of the aforementioned approaches (or at least reduce the risk of gross errors).

Conventional methods addressing body truncation and metal-induced artefacts in MR images rely on inpainting the missing regions (manually or semi-manually) (Schramm and Ladefoged 2019) or body contour estimation from the corresponding TOF PET-nonAC images (Qian *et al* 2012). However, a number of other strategies have been devised to address these issues in the context of PET/MRI. These include joint

estimation of attenuation and activity maps wherein the latent information about the attenuating medium in the raw PET data is extracted to account for metal artefact and/or body truncation (Mehranian *et al* 2016a). Moreover, direct attenuation and scatter correction in the image space using deep learning algorithms are also capable to mitigate the adverse impact of metal artefact and body truncation on PET images (Yang *et al* 2019, Dong *et al* 2020, Arabi *et al* 2020).

One of the limitations of this work is that only dental implants were considered for the simulation and evaluation of metal artefacts in MR images and the resulting PET AC maps. Other metallic implants, such as pedicle screws (spine fixation), shoulder joints, and hip prostheses would result in larger (in terms of volume) and more representative (in terms of location and shape) metal artefacts on MR image. As such, for full-scale validation of the proposed method, a wider range of metallic artefacts should be simulated and evaluated to cover common metal-induced errors in PET/MR imaging. The proposed method only predicts the missing underlying anatomical signals (in case of metal artefacts) to recover accurate body contour. However, metallic implants are overlooked in the resulting AC maps. This is a limitation imposed by the segmentation-based attenuation map generation method, which overlooks not only metallic implants but also bony structures. For PET/MRI scanners providing the option to use short-echo time (UTE) or zero-echo time (ZTE) MR sequences to generate PET AC maps, the training of the proposed method should be repeated using the same MR sequence. Moreover, since UTE and ZTE MR sequences are able to discriminate bony structures and exhibit less susceptibility to metallic implants, a similar framework could be adopted to not only recover the missing part of MR images but also predict the shape and location of metal implants for potential inclusion in the resulting PET AC maps. Very dense calcification might also lead to void signals in MR images, wherein similar approaches could be adopted to account for such dense calcification. For segmentation-based methods, when the void regions cause errors in the delineation of the body contour (or affect the boundary of the body), it is very challenging to identify accurately the body boundaries to discriminate the background air. However, when the void regions occur within the body without affecting/causing errors in body contour delineation, simple gap/hole filling algorithms could resolve this issue. This type of void regions could be challenging for the proposed method due to high variety of anatomical sites where dense calcifications could occur. Object completion models tend to estimate the missing regions through the information lying in the vicinity of the affected region. The metal implants usually replace the bony structures. Hence, the training of object completion models should focus mostly on these structures. However, when the void regions stem from dense calcification, the anatomical sites and the target organs might be different from metal-induced artefacts, and as such, a pertinent training dataset should be developed for this purpose.

5. Conclusion

A three-dimensional object completion approach was introduced to address body truncation and metal-induced artefacts in WB PET/MR imaging. This approach was capable of predicting semantic structures within the missing regions in MR images. Body truncation and metal artefacts in MR images translate to incomplete MRI-derived 3-class PET AC map and consequently remarkable underestimation of activity concentration in the corresponding PET images. The object completion approach was able to effectively recover the true body contour in MR images and improve the quantitative accuracy of PET images.

Acknowledgments

This work was supported by the Swiss National Science Foundation under grant SNRF 320030_176052, the Swiss Cancer Research Foundation under grant KFS-3855-02-2016 and the Eurostars programme of the European Commission under grant E! 12326 ILLUMINUS.

ORCID iD

Habib Zaidi https://orcid.org/0000-0001-7559-5297

References

Abdoli M, Mehranian A, Ailianou A, Becker M and Zaidi H 2016 Assessment of metal artifact reduction methods in pelvic CT *Med. Phys.* **43** 1588–97

Arabi H, Bortolin K, Ginovart N, Garibotto V and Zaidi H 2020 Deep learning-guided joint attenuation and scatter correction in multitracer neuroimaging studies *Hum. Brain Mapp.* **41** 3667–79

Arabi H, Dowling J A, Burgos N, Han X, Greer P B, Koutsouvelis N and Zaidi H 2018 Comparative study of algorithms for synthetic CT generation from MRI: consequences for MRI-guided radiation planning in the pelvic region *Med. Phys.* **45** 5218–33

Arabi H, Rager O, Alem A, Varoquaux A, Becker M and Zaidi H 2015 Clinical assessment of MR-guided 3-class and 4-class attenuation correction in PET/MR *Mol. Imaging Biol.* **17** 264–76

Arabi H and Zaidi H 2016a Magnetic resonance imaging-guided attenuation correction in whole-body PET/MRI using a sorted atlas approach *Med. Image Anal.* **31** 1–15

Arabi H and Zaidi H 2016b Whole-body bone segmentation from MRI for PET/MRI attenuation correction using shape-based averaging *Med. Phys.* **43** 5848

Arabi H, Zeng G, Zheng G and Zaidi H 2019 Novel adversarial semantic structure deep learning for MRI-guided attenuation correction in brain PET/MRI *Eur. J. Nucl. Med. Mol. Imaging* **46** 2746–59

Blumhagen J O, Braun H, Ladebeck R, Fenchel M, Faul D, Scheffler K and Quick H H 2014 Field of view extension and truncation correction for MR-based human attenuation correction in simultaneous MR/PET imaging *Med. Phys.* **41** 022303

Burger I A, Wurnig M C, Becker A S, Kenkel D, Delso G, Veit-Haibach P and Boss A 2015 Hybrid PET/MR imaging: an algorithm to reduce metal artifacts from dental implants in Dixon-based attenuation map generation using a multiacquisition variable-resonance image combination sequence *J. Nucl. Med.* **56** 93–97

Chen K T *et al* 2019 Ultra-low-dose ^{18}F-florbetaben amyloid PET imaging using deep learning with multi-contrast MRI inputs *Radiology* **290** 649–56

Dong X, Lei Y, Wang T, Higgins K, Liu T, Curran W J, Mao H, Nye J A and Yang X 2020 Deep learning-based attenuation correction in the absence of structural information for whole-body PET imaging *Phys. Med. Biol.* **65** 055011

Fuin N D, Pedemonte S D, Catalano O A, Izquierdo-Garcia D, Soricelli A, Salvatore M, Heberlein K, Hooker J M, Van Leemput K and Catana C 2017 PET/MR imaging in the presence of metal implants: completion of the attenuation map from PET emission data *J. Nucl. Med.* **58** 840–5

Gibson E *et al* 2018 NiftyNet: a deep-learning platform for medical imaging *Comput. Methods Programs Biomed.* **158** 113–22

Heußer T *et al* 2017 Investigation of the halo-artifact in 68Ga-PSMA-11-PET/MRI *PloS One* **12** e0183329

Hwang D, Kang S K, Kim K Y, Seo S, Paeng J C, Lee D S and Lee J S 2019 Generation of PET attenuation map for whole-body time-of-flight ^{18}F-FDG PET/MRI using a deep neural network trained with simultaneously reconstructed activity and attenuation maps *J. Nucl. Med.* **60** 1183–9

Ladefoged C N, Andersen F L, Kjaer A, Hojgaard L and Law I 2017 RESOLUTE PET/MRI attenuation correction for O-(2-^{18}F-fluoroethyl)-L-tyrosine (FET) in brain tumor patients with metal implants *Front. Neurosci.* **11** 453

Li W, Wang G, Fidon L, Ourselin S, Cardoso M J and Vercauteren T, 2017 On the compactness, efficiency, and representation of 3D convolutional networks: brain parcellation as a pretext task *Information Processing in Medical Imaging. IPMI 2017. Lecture Notes in Computer Science* vol 10265 ed M Niethammer *et al* (Berlin: Springer) pp 348–60

Lindemann M E, Oehmigen M, Blumhagen J O, Gratz M and Quick H 2017 MR-based truncation and attenuation correction in integrated PET/MR hybrid imaging using HUGE with continuous table motion *Med. Phys.* **44** 4559–72

Martinez-Moller A, Souvatzoglou M, Delso G, Bundschuh R A, Chefd'hotel C, Ziegler S I, Navab N, Schwaiger M and Nekolla S G 2009 Tissue classification as a potential approach for attenuation correction in whole-body PET/MRI: evaluation with PET/CT data *J. Nucl. Med.* **50** 520–6

Mehranian A, Arabi H and Zaidi H 2016a Quantitative analysis of MRI-guided attenuation correction techniques in time-of-flight brain PET/MRI *Neuroimage* **130** 123–33

Mehranian A, Arabi H and Zaidi H 2016b Vision 20/20: magnetic resonance imaging-guided attenuation correction in PET/MRI: challenges, solutions, and opportunities *Med. Phys.* **43** 1130–55

Mehranian A, Belzunce M A, McGinnity C J, Bustin A, Prieto C, Hammers A and Reader A J 2019 Multi-modal synergistic PET and MR reconstruction using mutually weighted quadratic priors *Magn. Reson Med.* **81** 2120–34

Meyer E, Raupach R, Lell M, Schmidt B and Kachelriess M 2010 Normalized metal artifact reduction (NMAR) in computed tomography *Med. Phys.* **37** 5482–93

Nuyts J, Bal G, Kehren F, Fenchel M, Michel C and Watson C 2013 Completion of a truncated attenuation image from the attenuated PET emission data *IEEE Trans. Med. Imaging* **32** 237–46

Ouyang J, Chun S Y, Petibon Y, Bonab A A, Alpert N and El Fakhri G 2013 Bias atlases for segmentation-based PET attenuation correction using PET-CT and MR *IEEE Trans. Nucl. Sci.* **60** 3373–82

Qian H, Manjeshwar R M, Ambwani S and Wollenweber S D 2012 Truncation completion of MR-based PET attenuation maps using time-of-flight non-attenuation-corrected PET images *2012 IEEE Nuclear Science Symp. and Medical Imaging Conf. Record (NSS/MIC)* (Piscataway, NJ: IEEE) pp 2773–5

Schramm G and Ladefoged C N 2019 Metal artifact correction strategies in MRI-based attenuation correction in PET/MRI *BJR Open* **1** 20190033

Schramm G, Langner J, Hofheinz F, Petr J, Lougovski A, Beuthien-Baumann B, Platzek I and van den Hoff J 2013 Influence and compensation of truncation artifacts in MR-based attenuation correction in PET/MR *IEEE Trans. Med. Imaging* **32** 2056–63

Schulz V *et al* 2011 Automatic, three-segment, MR-based attenuation correction for whole-body PET/MR data *Eur. J. Nucl. Med. Mol. Imaging* **38** 138–52

Shen L, Zhao W and Xing L 2019 Patient-specific reconstruction of volumetric computed tomography images from a single projection view via deep learning *Nat. Biomed. Eng.* **3** 880–8

Smith L N 2018 A disciplined approach to neural network hyper-parameters: part 1–learning rate, batch size, momentum, and weight decay (arXiv:1803.09820)

Wollenweber S D, Ambwani S, Lonn A H, Shanbhag D D, Thiruvenkadam S, Kaushik S, Mullick R, Qian H, Delso G and Wiesinger F 2013 Comparison of 4-class and continuous fat/water methods for whole-body, MR-based PET attenuation correction *IEEE Trans. Nucl. Sci.* **60** 3391–8

Yang J, Park D, Gullberg G T and Seo Y 2019 Joint correction of attenuation and scatter in image space using deep convolutional neural networks for dedicated brain ^{18}F-FDG PET *Phys. Med. Biol.* **64** 075019

Zaidi H and Becker M 2016 The promise of hybrid PET/MRI: technical advances and clinical applications *IEEE Sign. Proc. Mag.* **33** 67–85

Zaidi H, Ojha N, Morich M, Griesmer J, Hu Z, Maniawski P, Ratib O, Izquierdo-Garcia D, Fayad Z A and Shao L 2011 Design and performance evaluation of a whole-body Ingenuity TF PET-MRI system *Phys. Med. Biol.* **56** 3091–106